Extrasolar planet detection through spatially resolved observations

Meshkat, T.R.

Citation

Meshkat, T. R. (2015, June 11). *Extrasolar planet detection through spatially resolved observations*. Retrieved from https://hdl.handle.net/1887/33272

Author: Meshkat, Tiffany
Title: Extrasolar planet detection through spatially resolved observations
Issue Date: 2015-06-11

Chapter 1

INTRODUCTION

The interest in extrasolar planets (exoplanets) has been a feature of human inquiry for thousands of years, as evidenced by Epicurus' letter to Herodotus in the 4th century B.C. where he postulated that many other worlds – similar and different to our own – must exist. This curiosity is very relatable: we want to better understand ourselves, our planet, and our place in the universe. Until fairly recently, the only known planets were in our own solar system. Much of star and planet formation theories were derived from this limited knowledge. The existence of exoplanets was only confirmed when indirect planet detection techniques became suitably sensitive to find planets (Wolszczan & Frail 1992; Mayor & Queloz 1995).

The earliest exoplanet detection technique, radial velocity, takes advantage of the subtle Doppler shift in a star's spectrum due to a massive body orbiting nearby. This gravitational "wobble" technique revealed hundreds of close-in planets with systems very different to our own. The existence of "Hot Jupiters", planets as massive as Jupiter but within Mercury's orbit, led to a whole new field of planet migration studies. Later on, the transit technique led to the discovery of hundreds more planets which, by chance alignment with Earth, block out a small amount of the light from a star, causing a dip in its light curve over time. Since then, technological developments both from the ground and space, have resulted in the discovery of >1500 confirmed planets[1], in a diverse range of architectures and masses. The size and distribution of exoplanets around nearby stars in our galaxy provides insight into the different types of planet formation. This ultimately can help to reveal if our Solar System is typical or an exception.

---

[1] exoplanets.org

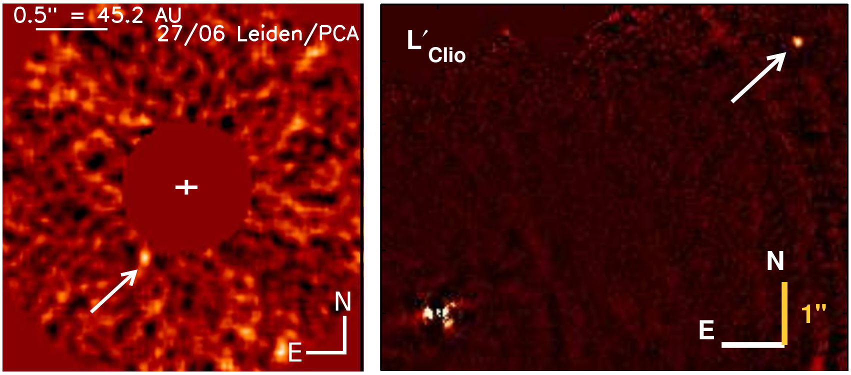

Figure 1.1 Left: Directly imaged 5 Jupiter mass planet HD 95086 b from Rameau et al. (2013c), indicated with a white arrow. Right: Planet HD 106906 b (white arrow) L'-band detection from Bailey et al. (2014).

1.1 Directly Imaging Exoplanets

Direct imaging is a recently successful technique to detect and characterize exoplanets. It involves directly detecting the photons from a planet itself. This techniques provides a unique opportunity to study young planets in the context of their formation and evolution. It examines the underlying semi-major axis exoplanet distribution (5 to 100 AU) and enables the characterization of the planet itself with spectroscopic examination of its emergent flux (Konopacky et al. 2013).

This method of planet detection is challenging for several reasons, some of which are readily apparent (planets are small, faint, and close to their host star) and others which are less clear from the outset (such as wavefront control, quasi-static speckles, etc. see Section 1.4). The limits of current technology only allow the direct detection of young, self-luminous planets. These young planets are still warm from their contraction, making them easier to directly detect in the infrared (Burrows et al. 2004) with typical planet-to-star contrasts of $10^{-5} - 10^{-6}$, compared to the values of $10^{-9} - 10^{-10}$ for more mature planets. Since these planets are young, they are ideal candidates to study the late stages of planet formation.

Despite the technical challenges associated with these detections, a handful of planetary-mass companions have been detected and confirmed (Figure 7.3): HR8799 bcde (Marois et al. 2008, 2010), Fomalhaut b (Kalas et al. 2008), β Pic b (Lagrange et al. 2009, 2010), 2MASS1207 b (Chauvin et al. 2004), 1RXS J1609–2105 b (Lafrenière et al. 2008), HD 95086 b (Rameau et al. 2013a), HD 106906 b (Bailey et al. 2014), GJ 504 b (Kuzuhara et al. 2013), and GU Psc b (Naud et al. 2014). A few of the detections may even be planets caught in formation (LkCa 15 b: (Kraus & Ireland 2012), HD 100546 b: (Quanz et al. 2013)). The detections of these young planets are beginning to bridge the gap between planets at large orbits (such as giant and icy giant planets in our Solar System) and their cooler and later stage cousins which are well mapped by the radial velocity and transit techniques.

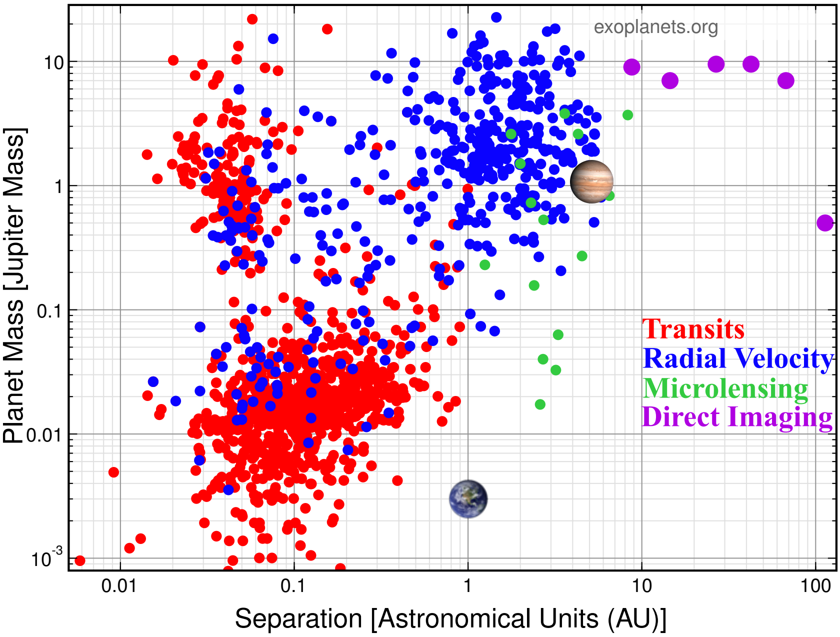

Figure 1.2 All detected and confirmed planets shown as a function of planet-star separation in AU and Jupiter masses (from exoplanets.org). The different colored points denote the method the planet was originally detected in. The vast majority of planets have been detected through the transit (red) and radial velocity (blue) method. Directly imaged planets (purple) are at a wider separation and higher mass than those detected through other techniques. Earth and Jupiter are also included as reference points.

Figure 1.2 shows the known and confirmed exoplanets, color coded based on the detection technique (from exoplanets.org). The planet-star separation in AU is plotted against the planet mass in Jupiter masses. Most of the planet detections have been made with the radial velocity (blue) and transit (red) method. Those two methods also overlap in planet-star separation and planet masses, allowing some targets to be observed via both methods. The direct imaging (purple) technique has only a handful of confirmed detections, at relatively high planet masses and large planet-star separations. Though there are fewer directly imaged planets, they occupy a previously unexplored region of this diagram. These planets are also very young, and thus probe earlier stages of planet formation, complementing the planets detected through other techniques. Advances in optics, wavefront control, and image processing techniques allow us to probe for lower mass, closer-in planets.

1.2 Planet Formation

Stars are formed from large cold clouds of molecular gas. Gravitational instability perturbs the cloud and starts its collapse. As a star forms out of a molecular cloud (Bergin & Tafalla 2007), conservation of angular momentum flattens its surrounding dust and gas into a circumstellar disk. It is in this early, gas rich stage that planets are thought to form. Eventually the gas is depleted, either blown out into the interstellar medium through stellar winds or through accretion onto the star or a planet (Alexander et al. 2014). The final stage in the disk life around a star is the debris disk phase, where planetesimals are collisionally ground up to form dust that is seen in reflected light (reviews by Wyatt 2008; Matthews et al. 2014). The planets in debris disks are thus recently formed, but the formation mechanism of giant planets is still a matter of contention. Even Jupiter's interior (and thus formation mechanism) is not well understood (Guillot 2005; Fortney & Nettelmann 2010). Two of the most popular giant planet formation mechanisms are core accretion (Safronov & Zvjagina 1969; Hayashi 1981; Pollack et al. 1996) and gravitational instability (Boss 1998; Mayer et al. 2002).

Core accretion begins with small micron and centimeter sized particles in a disk colliding and sticking together to form larger particles. These particles eventually coagulate to form planetesimals, which accrete to form a rocky planetary core ($\sim 5-10 M_{\oplus}$). As this planetary core orbits the star, its gravity accretes gas onto the surface of the core in a runaway process. This sweeping-up process also may explain how planets migrate through a disk. Planetary migration is a process which must have occurred given the observations of "Hot Jupiters" , which are too massive to have formed and swept-up enough gas at their current, small orbital separations (Lin et al. 1996; Rasio et al. 1996). However, this formation method is not without its challenges. Meter sized particles are expected to collide at velocities that are too high to result in sticking (Brauer et al. 2008). These bodies also decouple from the gas, causing them to drift rapidly into the star (Weidenschilling 1977). These two processes make it difficult for particles to grow larger than a meter in size. Icy dust grains have been proposed as a method to overcome this barrier, as ice grains collide and stick more easily (Okuzumi et al. 2012; Krijt et al. 2015). Also, accretion of gas onto the core must occur before the disk dissipates. Core accretion is thought to occur on a timescale of 0.5 to 10 Myr, while the observed disk lifetimes are 1 to 10 Myr.

Gravitational instability is a "top-down" method of giant planet formation. A higher mass planet is thought to form out of an instability in the gas and dust rich disk, which fragments into clumps and starts a gravitational collapse (Boss 1998; Mayer et al. 2002). In this scenario, the dust grains sink to form the core of the planet via self-gravity. Unlike core accretion, gravitational instability can form planets relatively quickly, with a timescale of a few disk orbits (100-1000 years at 10 to 100 AU). However, the cause of the fragmentation is uncertain. Fragmentation can only occur if the disk cools quickly enough, based on the Toomre instability parameter, or it can be caused by an external gravitational trigger, such as a binary star (Mayer et al. 2005).

Boley (2009) proposed that both planet formation mechanisms may create

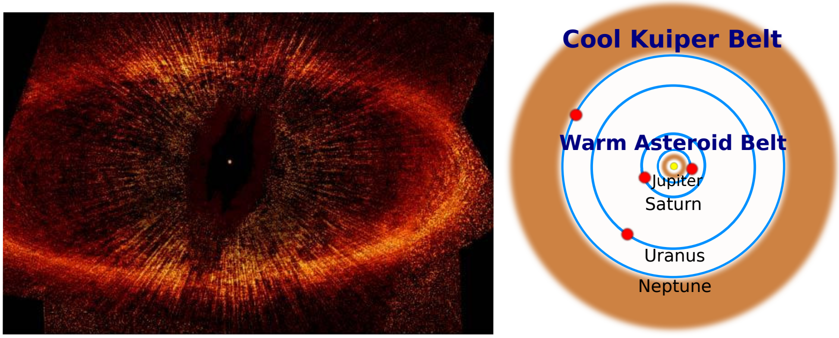

Figure 1.3 Left: The debris disk around the star Fomalhaut (Kalas et al. 2005), seen with the Hubble Space Telescope in scattered light. The debris has been sculpted into a ring, likely by an unseen planet. Right: Visualization of the two-belt dust debris structure in the Solar System.

planets in different parts of the disk: gravitational instability beyond a disk radii $r > 100$ AU and core accretion inside $r < 100$ AU. Transit studies with the Kepler space telescope have revealed that small planets ($\leq 2.5 R_{\oplus}$) are extremely common at small angular separations (Batalha et al. 2013; Fressin et al. 2013; Lissauer et al. 2014). Given their current separation and relatively low mass, most of these planets are thought to have formed via core accretion. Direct imaging surveys suggest that planets are very infrequent at large separations (see Section 1.5). These large separation, high mass planets have been proposed to form by gravitational instability (Marois et al. 2010). However, recent studies cast doubt on the HR 8799 planets having formed via gravitational instability, as their masses and separations do not fulfill the model Toomre and cooling time criteria (Rameau et al. 2013a). Additionally, the lack of giant planets at large orbital radii suggests that giant planets formed via gravitational instability are uncommon (Bowler et al. 2015).

Theoretical planet cooling curves are employed to predict the temperature of giant planets over time. The “hot-start” models (Burrows et al. 1997) are most closely related to the gravitational instability planet formation mechanism: an object radiates its initial gravitational potential energy slowly. The “cold-start” and “warm-start” models (Marley et al. 2007; Spiegel & Burrows 2012) involve the rapid loss of initial entropy caused by accretion, and thus is more related to core accretion. The masses of directly imaged planets are estimated from these evolutionary models.

1.3 Planet-Disk Interactions

In addition to detecting and characterizing planets, the results of direct imaging studies contribute to our understanding of debris disks. Nearly all of the directly imaged planets have been found around stars with debris disks; bright circumstellar dust clouds (see Figure 1.3, left). The dust is generated in collisional cascades of

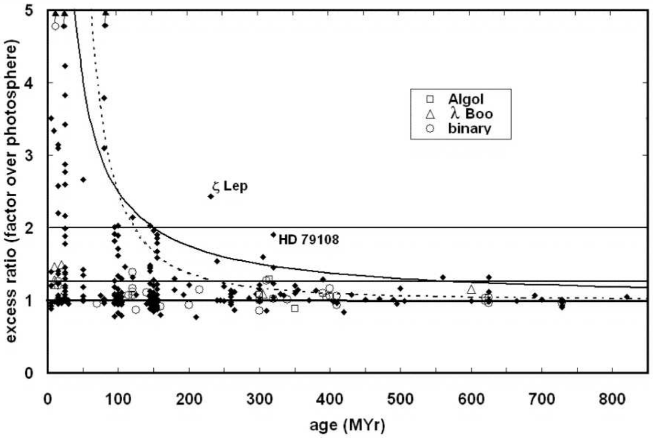

Figure 1.4 24 μm excess emission versus age for A-type stars, from (Rieke et al. 2005). The excess emission is the ratio of the flux density in the SED over the stellar photosphere alone. A ratio of 1 has no excess emission. Targets with an excess ratio >1.25 are considered the threshold for detection of an excess. An excess ratio >2 is considered a large excess. The decaying frequency of debris disks with age demonstrates the likelihood that an A-type star with a debris disk is young.

asteroids and comets, which can form grains down to a few microns (Acke et al. 2012). These small bodies are the remnants of planetesimals, which are thought to be the building blocks of planet cores. Thus, debris disks may be indicators of recent planet formation.

Debris disks can be directly detected (Figure 1.3, left) or inferred from excess infrared emission in a stellar energy distribution (SED). Resolved debris disks are extremely useful for direct imaging studies, as the inclination of the system can be assessed and, in some cases, substructure (such as gaps or holes) can be seen (Kalas et al. 2005). If a companion is detected in such systems, the inclination allows determination of the orbital separation from the star, rather than the projected separation. For unresolved debris disks, the approximate mass, temperature, inner and outer radii can be inferred by fitting the SED with an appropriate model. Figure 1.4 demonstrates that the frequency of debris disks decays over time (Rieke et al. 2005). These debris disks are inferred from excess 24 μm emission in their SEDs. Whether the disk is resolved or not, debris disks provide a wealth of information about the structure of the dust around a star and imply youth for the system.

A subset of debris disks show the signature of two temperature components in the SED: a warm inner belt and a cool outer belt. The relatively dust-free gap between these belts may be caused by one or more planets accreting the debris material as they form (Chiang et al. 2009). Our own Solar System has a two-component structure, with a warm inner asteroid belt, cool outer Kuiper belt, and

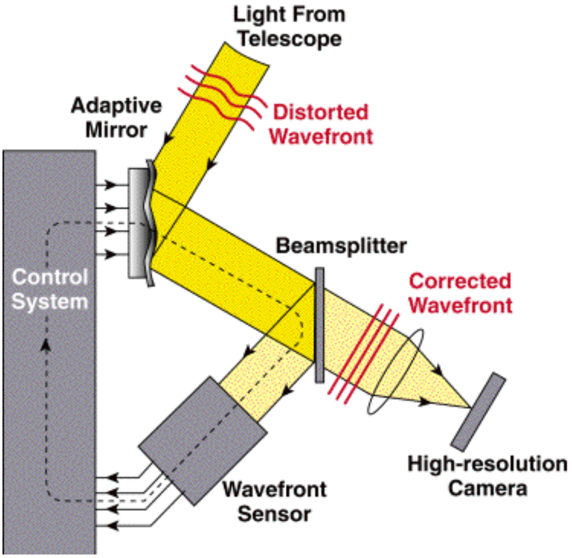

Figure 1.5 Demonstration of how an AO system corrects an incoming wavefront using a wavefront sensor which then adjusts the deformable mirror in real-time to produce a final corrected image (lyot.org).

four planets present across the gap (Figure 1.3, right). In the case of Fomalhaut, the cool outer belt is resolved, while the warm inner belt is inferred from the SED.

1.4 Observing Strategies and Image Processing

1.4.1 Optical Aberrations

As the light from a point source passes through an optical system, the shape of the image is called the point spread function (PSF). In the case of a circular aperture in a telescope, the PSF shape is described as an Airy disk. The central core of the PSF contains most of the stellar flux, with several, successively fainter Airy rings around the star. The theoretical, diffraction-limited resolution of a telescope is defined on this basis:

$$\theta \approx 1.22\lambda/D \tag{1.1}$$

where λ is the wavelength and D is the diameter of the telescope. This also defines the minimum angular separation at which two objects of equal brightness can be resolved. Reaching this limit at a telescope, the so-called “Diffraction limit”, is the goal if one wants to detect objects very near each other (i.e. planets). In order to reach a smaller diffraction limit, one must either observe in a shorter wavelength or with a larger telescope.

Achieving the diffraction limit of a telescope, however, is a challenging task. Instrumental aberrations are present in nearly every optical system. Even the Hubble Space Telescope has spherical aberrations in the primary mirror. In addition to static instrumental aberrations, ground-based telescopes have the challenge of observing through the turbulent, refractive atmosphere of the Earth.

1.4.2 Adaptive optics

The Earth's atmosphere introduces temporal and spatial variations in the light path from a point source, causing an image to appear smeared out. Adaptive Optics (AO) was invented in order to counter this blurring. An AO system measures the deviations in the incoming stellar wavefront using a wavefront sensor. The wavefront sensor determines the correction necessary to create a flat wavefront, and sends the correction information to a deformable mirror (DM). Ideally the DM cancels the aberration in the wavefront by physically reshaping the mirror, using actuators, to be the inverse aberration shape with half the amplitude. In a theoretical system where the DM is able to correct the atmospheric aberrations in real-time, the resulting wavefront would be flat. In practice, there is a brief time delay between the wavefront sensor and the DM correction. This process is repeated hundreds of times a second in order to compensate for the varying turbulence, which produces a point source (see Figure 1.5).

In order for this process to measure the wavefront accurately, a bright light source is needed. If the target object is too faint to be a natural guide star, a laser guide star is used to generate a fake point source. For the purposes of directly imaging exoplanets, the target stars are most often bright enough to act as their own natural guide star. AO correction is necessary to directly image exoplanets, since we require the stellar flux to be centralized in a point source as much as possible, in order to detect faint point sources at very small angular separations.

1.4.3 Coronagraphs

Coronagraphs are optics inserted in the light path of a telescope which minimize the diffracted light from a source, to allow access to small angular separations around a star. One of the first coronagraphs, the classical Lyot (Lyot 1939), achieved this with two optical elements, visualized in the top light path diagram in Figure 1.6. The light from the star (blue line) is blocked by a mask in the focal plane of the telescope. Since the planet (red line) is physically separated from the star, the angle of its incoming light is not blocked by the mask. Then a Lyot stop is inserted in the pupil plane in order to block the outer edge of the telescope pupil in the pupil plane image. Finally the image is formed on the detector. This coronagraph design is extremely sensitive to the telescope alignment, as the star must be placed precisely behind the focal plane mask (called tip-tilt alignment) and is thus sensitive to telescope vibrations. This physical mask also has the potential to block a planet signal, which may be very close to its parent star. Developments in coronagraphs have led to significant improvements on the classical Lyot (4QPM; Rouan et al. 2000), however the tip-tilt alignment is still a limitation as most

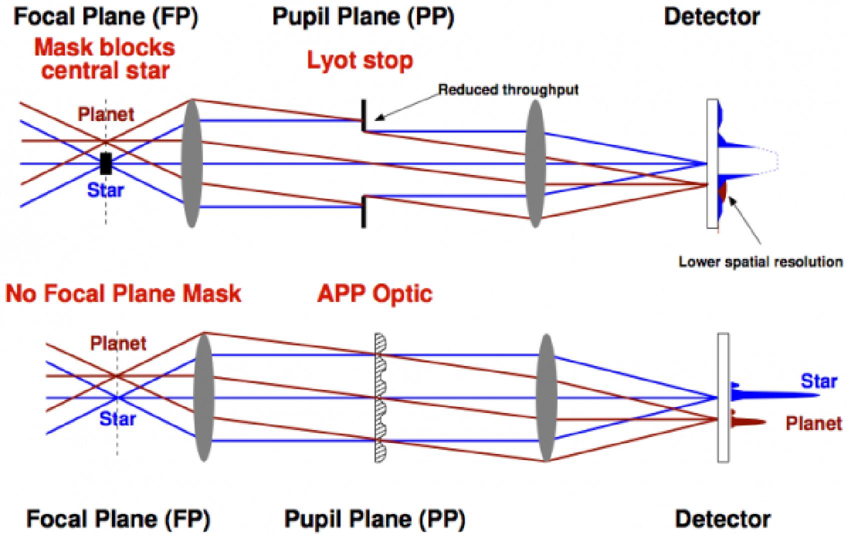

Figure 1.6 Light path diagrams demonstrating the Lyot coronagraph and the APP coronagraph designs, from Kenworthy et al. (2010). Both coronagraphs aim to allow the detection of faint sources close to a bright star. The classical Lyot uses a focal plane mask and a Lyot stop in the pupil plane. The APP only has one optic, which is in the pupil plane. The resulting image on the detector is seen on the right.

designs require an optic in the focal plane.

The Apodizing Phase Plate (APP) coronagraph (Kenworthy et al. 2010) uses only a single optic, placed in the pupil plane of the telescope, seen in the bottom light path diagram in Figure 1.6. The APP optic uses the light diffracted from the Airy core of the star to cancel out the coherent light in the diffraction rings. In effect, this minimizes the diffraction pattern on one side of the star, while reinforcing it on the other side. The result is seen on the right of Figure 1.6, the central Airy core of the star still reaches the detector, but the adjusted diffraction ring pattern allows the planet signal to shine through. This figure also demonstrates that everything in the field of view will have the characteristic APP diffraction suppression structure, including planets. As the central Airy core flux itself is used to cancel out the diffraction pattern on one side of the star, there is a cost of 40% to throughput. The APP was designed to have a “dark hole” where the sky background limit can be reached in the final APP images from $0\farcs18$ to $0\farcs75$ in which to search for faint companions. The most significant difference with previous coronagraph design is the lack of a focal plane mask. Thus, the APP is insensitive to tip-tilt errors and can even be used to observe binary star systems. Figure 1.7 shows the increased sensitivity at small angular separations with the APP (solid line), compared with direct imaging (dashed line). This figure was generated using real archival data of the same target obtained in L'-band with the

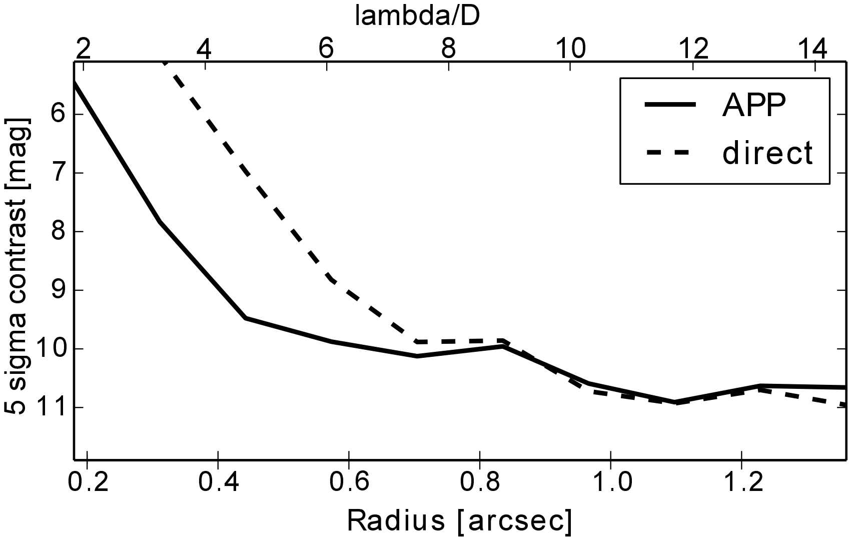

Figure 1.7 Comparison of sensitivity achieved with the APP coronagraph versus direct imaging for the same target observed with the NACO instrument on the VLT (from Meshkat et al. *submitted*).

NACO instrument on the VLT and processed with these same pipeline.

1.4.4 Angular Differential imaging

Sophisticated image processing algorithms are necessary to remove the "quasi-static super speckles" in our data, in order to let the light from a planet shine through. Though direct imaging data are obtained with AO correction, speckles remain in the images. These speckles, caused by instrumental features and residual atmospheric turbulence, can appear brighter than a planetary-mass companion (Hinkley et al. 2009). Several image processing algorithms have been developed to model and subtract these aberrations. One such algorithm is Angular Differential Imaging (ADI: Marois et al. 2006). In ADI mode, the sky de-rotator on an ALT-AZ mounted telescope is turned off, allowing the sky to rotate around a star. A planet will appear to orbit over time, while the aberrations stay relatively fixed. Assuming the planet is not in the same position in any consecutive images, a median over all images in time will capture the static speckle aberrations, but not the planet. While this median image succeeds in modelling the general stellar PSF structure, the speckles vary in brightness on time scales of the observing sequence.

1.4.5 SDI

Based on evolutionary cooling tracks (Baraffe et al. 2003), planets were predicted to have a strong methane signal, similar to field brown dwarfs. Simultaneous

Differential Imaging (SDI) is a method which takes advantage of this prediction, by simultaneously imaging in and out of the methane absorption feature at 1.62 μm. By subtracting the different narrow-band images, the stellar flux and speckles will be subtracted and the light from planet with methane absorption will be preserved (Biller et al. 2007). However, many recent studies do not find strong methane absorption from the known directly imaged planets (e.g. HR 8799 bcd and 2M1207 b; Skemer et al. 2014), suggesting that planets are not the same as field brown dwarfs of equivalent effective temperatures.

1.4.6 Locally optimized combination of images

Locally Optimized Combination of Images (LOCI) (Lafrenière et al. 2007) is a planet detection algorithm which models the stellar PSF in a subregion of the images to remove speckles. Data are obtained in ADI mode, to allow any companion source (and the sky) to rotate between successive images in time. For the ADI algorithm a simple median is taken over all the images in order to subtract the stellar PSF. This assumes that there is enough sky rotation such that a companion will never overlap with itself in successive images. In practice, a companion will always have some small amount of overlap between images. Thus, subtracting the median of the images will result in some self-subtraction of a companion. The LOCI algorithm mitigates this problem by introducing the parameter N_δ, which is the minimum amount of overlap allowed in units of the PSF full-width half maximum (FWHM). This determines how many images are rejected from the stellar PSF fit, in order to prevent self-subtraction. For example, an N_δ of 1 ensures there is no overlap of a companion, however it may result in the rejection of many frames depending on the sky rotation and angular separation of a companion. At smaller angular separations, the same amount of sky rotation results in a smaller actual movement:

$$\text{linear motion} = 2\pi \text{r} \frac{\theta}{360^\circ} \tag{1.2}$$

At very small angular separations (r), a companion may have very little linear motion, resulting in many rejected images. Lafrenière et al. (2007) consider a range of N_δ values from 0.25 (much self-subtraction allowed) up to 2.0 (none allowed). They find the value of N_δ=0.5 is optimal trade-off at including enough images to generate an accurate stellar PSF model while preventing too much self-subtraction.

The LOCI algorithm differs further from ADI by not taking a simple median over the images. The images are divided into annuli, which are subdivided into wedges. A linear least squares combination of images subtracts the speckles within one wedge region at a time. The size of each wedge is based on two parameters set by the user. This wedge is called the signal region S_T, where a potential planet signal is considered. As the sky rotation causes the planet to rotate around its parent star, it will pass in and out of the S_T region over the whole observing sequence. A larger optimization region wedge O_T, usually surrounding S_T, is used as a reference for speckles at that location. A least squares fit is performed on O_T at a fixed pixel location over the whole set of observed frames. Since the sky is rotating around the parent star, a planet would only appear temporarily in the wedge in a few frames and therefore will not be a significant contribution to the least squares fit. To minimize the self subtraction of a potential planet, the frames nearest in time to a given single science frame are not included in the least squares fit. The fit of the O_T region is subtracted from the S_T region, and the process is repeated for all other wedges. Once all the wedges are processed, the frames are rotated by the parallactic angle so all the frames have the North axis up and East to the left. This least squares fitting algorithm is successful at minimizing speckles, however at small angular separations the self-subtraction is still an issue.

1.4.7 Principal Component Analysis

Principal Component Analysis (PCA) is another algorithm whose recent application to high contrast exoplanet imaging has been shown to be very effective (Amara & Quanz (2012), Soummer et al. (2012)). For exoplanet imaging, PCA involves converting a stack of science images into principal, orthogonal, linearly uncorrelated components. Some linear combination of these basis vectors, called principal components (PCs), can be used to represent every science image in the original stack.

PCA also takes advantage of data obtained in ADI mode, though sky rotation is not strictly necessary [2]. Unlike LOCI, the whole image is processed at once, rather than subdivided into wedges, making PCA less expensive. All the images in a stack are flattened into a single dimensional array. The mean of the stack of flattened images is subtracted from each flattened image. This step ensures the computed PC vectors always go through the origin. The flattened images are passed to a singular value decomposition (SVD) algorithm in order to determine the most dominate features in the images. SVD returns the following three matrices:

$$S = UWV^T \tag{1.3}$$

where S is the stack of one-dimensional images, U is a column-orthogonal matrix, W is a diagonal matrix with the positive, singular values corresponding to each PC, and V contains the PC singular vectors. The n^{th} PC singular value is the variance of the image stack in the direction of the n^{th} PC vector. The PCs are in order of decreasing contribution. The first PC has the highest singular value and defines the direction of the line through the origin that best fits the derived stack of images, in a least squares sense. A subset of these PCs are used in the linear least squares fit. The mean of the stack of flattened images, which was subtracted earlier, is appended to this subset of PCs. A linear least squares fit of this subset of PCs is performed on the first flattened image. The resulting coefficients are crossed with the PCs to construct the stellar PSF for the first image. The stellar PSF model is subtracted from the first image. This process is repeated for all subsequent images. The optimal number of PCs used in the linear fit is a trade-off between subtracting speckles and increasing the background noise.

---

[2] demonstrated with the equatorial mounted Palomar telescope, see (Fergus et al. 2014).

1.5 Overview of Direct Imaging Surveys

Many surveys have been performed, taking advantage of technological and image processing advantages (section 1.4), in order to directly image planets. There are several, large completed imaging surveys, each of which imaged ~40 to 250 stars: the Gemini Deep Planet Survey (GDPS, Lafrenière et al. 2007, the L' and M-band survey of sun-like stars (Heinze et al. 2010), the International Deep Planet Survey (IDPS, Vigan et al. 2012), the NICI instrument science campaign (Biller et al. 2013; Wahhaj et al. 2013; Nielsen et al. 2013), the NACO L'-band survey (Rameau et al. 2013a), the Strategic Exploration of Exoplanets and Disks with Subaru (SEEDS, Janson et al. 2013; Brandt et al. 2014), the NACO instrument large program (Desidera et al. 2015; Chauvin et al. 2015) the Planets around Low-mass Stars (PALMS) survey (Bowler et al. 2015). Despite the huge amount of stars surveyed, only three planetary systems were discovered through these surveys: HR 8799 bcde (Marois et al. 2008, 2010) from the GDPS survey, HD 95086 b (Rameau et al. 2013b) from the NACO L'-band survey, and GJ 504 b (Kuzuhara et al. 2013) from the SEEDS survey. Despite the few planet detections, many of these surveys have performed robust statistical analyses in order to place constraints on the planet occurrence rate as a function of stellar properties. The key findings and statistics from each survey are reported below.

GDPS was one of the first large direct imaging surveys searching for planets. 85 FGKM-type stars were observed at the Gemini North with the NIRI instrument in the narrowband filter CH4-short (1.54-1.65 μm) with ADI and AO (see Section 1.4). The data on average were sensitive to planets down to 2 M_{Jup} with a projected separation of 40 to 200 AU. Many companion candidates were detected in the initial analysis, but nearly all of the second-epoch observations confirmed that these were background sources (48 out of 54 targets). This high false-positive rate is a common occurrence for data in the 1.6 μm range, as stars are brighter in these shorter wavelengths. The remaining targets were discovered to be binary companions. The HR 8799 four planets were reported separately from the survey paper (Marois et al. 2008, 2010). They found the upper limit of the fraction of stars with at least one planetary mass object is 0.28 for 10-25 AU, 0.13 for 25-50 AU, and 0.093 for 50-250 AU.

The L'- and M-band survey obtained data no 54 nearby, sun-like stars with the Clio instrument on the MMT. The targets were preferentially selected based on proximitymed to be background stars. targets. Thirteen potential companions were detected, eleven of which were confirmed to be background stars. A low-mass star and brown dwarf companion were discovered, but no planetary mass objects were detected. They performed Monte Carlo simulations to test the planet distribution power law coefficients (Heinze et al. 2010a), assuming radial velocity statistics. They conclude that less than 8.1% of stars have three, wide orbit, massive planets, like the HR 8799 system. Thus, giant planets in large orbital separations are rare around sun-like stars.

The IDPS survey combined data from the VLT/NACO instrument and Gemini/NIRI instrument on 42 A-type stars with the CH4s and Ks-band (1.95-2.30μm) filters. A-stars are often the targets in direct imaging surveys, as radial velocity searches for planets (Johnson et al. 2007) and planet formation theories (Alibert et al. 2011) suggest that more massive stars form massive planets more frequently. No planetary mass companions were detected in this survey. Their statistical analysis of the null result concludes that the fraction of A-stars with one massive planet (3-14 $M_{\rm Jup}$) is 5.9-18.8% from 5-320 AU at 68% confidence. They suggest that the peak of the massive planet population around A-stars may fall between the separations probed with radial velocity and direct imaging.

The NICI science campaign used the Gemini/NICI instrument in H-band to determine the frequency of giant planets around three surveys of stars: 57 debris disk stars, 80 young moving group stars, and 70 young B and A stars. Many companion candidates were detected in these surveys, but follow-up confirmed that all were either background sources, brown dwarfs or stellar mass companions. Bayesian analysis of the null result in the young moving group survey of 80 stars resulted in the strongest constraint on the planet fraction at that time: $\leq$6% of stars have 1-20 $M_{\rm Jup}$ planetary mass objects at semi-major axes of 10-150 AU at the 95% confidence level, using COND models (Baraffe et al. 2003). The debris disk survey concluded that the β Pic and HR 8799 planetary systems are rare. The B and A star survey agreed with this analysis: <10% of B and A stars have a planetary mass companion similar to the outer-most HR 8799 planet b (7 $M_{\rm Jup}$ at 68 AU) at 95% confidence.

The NACO L'-band survey (Rameau et al. 2013a) targeted 59 young, nearby stars with inferred debris disks with the VLT/NACO instrument in L'-band (3.8μm). The HD 95086 b planet was reported separately from the survey paper (Rameau et al. 2013b). Based on their survey results, their statistical analysis of the fraction of giant planets at large separations finds that 1-13 $M_{\rm Jup}$ planets have an occurrence of 10.8% to 24.8% from 1-1000 AU, at 68% confidence level.

The SEEDS survey is not yet complete. The results published thus far combine observations of ~250 stars with the Subaru/HiCIAO, Gemini/NIRI, and Gemini/NICI instruments. All data were obtained in H-band (1.65μm). The detection of the planet GJ 504 b was published separately (Kuzuhara et al. 2013). Through statistical analysis of their sample, they find that the commonly used radial velocity planet distribution function cannot extend beyond the (model-dependent) maximum semimajor axis of 30-100 AU.

The NACO large program observed 86 FGK-type stars with the VLT/NACO instrument in H-band, aiming to provide constraints on the frequency of planets and brown dwarfs in preparation for the new VLT/SPHERE instrument. No new planets were detected as part of this survey. They determine an upper limit on the occurrence of giant planets to be <15% for a >5 $M_{\rm Jup}$ planet between 100-500 AU, and <10% for a >10 $M_{\rm Jup}$ planet between 50-500 AU at 95% confidence.

The PALMS survey targeted 122 young M dwarf stars with H and K-band coronagraphic observations with the Keck/NIRC2 and Subaru/HiCIAO instruments. Four new brown dwarf companions were discovered, but no planetary mass objects were detected. The null results were used to provide the first statistical constraints on the occurrence of giant planets around M dwarfs, with an upper limit of 10.3% and 16.0% for 1-13 $M_{\rm Jup}$ planets between 10 and 100 AU for the hot-start (Burrows et al. 1997) and cold-start (Marley et al. 2007) evolutionary models, at the 95%

Survey	Bands	N_{star}	Spectral Types	Statistical results
GDPS (Lafrenière et al. 2007)	CH4s	85	FGKM	fraction of stars with at least one planetary-mass object is 0.28 for 10-25 AU, 0.13 for 25-50 AU, and 0.093 for 50-250 AU
L' and M-band survey of sun-like stars (Heinze et al. 2010)	L' and M	54	FGK	<8.1% of stars have three, wide orbit, massive planets
IDPS (Vigan et al. 2012)	CH4s and Ks	42	A	fraction of A-stars with one massive planet (3-14 M_{Jup}) is 5.9-18.8% from 5-320 AU, 68% confidence
NICI (Biller et al. 2013; Wahhaj et al. 2013; Nielsen et al. 2013)	H	~80	BAFGKM	≤6% of stars have 1-20 M_{Jup} planetary-mass objects at semi-major axes of 10-150 AU, 95% confidence
NACO L'-band survey (Rameau et al. 2013a)	L'	59	BAFGKM	1-13 M_{Jup} planets have an occurrence of 10.8% to 24.8% from 1-1000 AU, 68% confidence
SEEDS (Janson et al. 2013; Brandt et al. 2014)	H	~250	BAFGKM	RV planet distribution function cannot extend beyond the maximum semimajor axis of 30-100 AU, 95% confidence
NACO large program (Desidera et al. 2015; Chauvin et al. 2015)	H and Ks	86	FGK	<15% for a >5 M_{Jup} planet between 100-500 AU, and <10% for a >10 M_{Jup} planet between 50-500 AU, 95% confidence
PALMS (Bowler et al. 2015)	H and K	122	M	<10.3% and 16.0% for 1-13 M_{Jup} planets between 10 and 100 AU for hot-start and cold-start models, 95% confidence

Table 1.1 Summary of all major direct imaging surveys, including the planet frequency models ruled out due to statistical analysis.

confidence level.

Table 1.1 compares the targets, observations, and summarizes the results of these surveys. Except for the NACO L'-band survey, these surveys all obtained data in the near infrared (H and Ks-band). Theoretical evolutionary models predicted that planets would have strong methane absorption and little cloud opacity, similar to field brown dwarfs (COND; Baraffe et al. 2003). Thus, detecting a planet in methane absorption was one of the driving motivations for observing in H and Ks-band, rather than longer wavelengths. However, most directly imaged planets do not show evidence of methane absorption (HR8799bcd, 2M1207b; Skemer et al. 2014) and are redder than expected (Galicher et al. 2014), unlike field brown dwarfs of similar effective temperatures. This is likely a contributing factor to the low planet detection rate in these surveys. Additionally, nearly all these surveys agree that the massive, large orbital separation planets around HR 8799 and β Pic are rare.

1.6 This Thesis

The work presented in this thesis aims to build upon the results from previous direct imaging surveys, learning both from the target selection and planet frequency models, while also taking advantage of technological advances. This thesis presents an optimized image processing algorithm, the results of two surveys searching for planets, a significant non-detection of a known planet, and a new detection of an M-dwarf.

Chapter 2
Directly detecting the signal from a very faint planet next to a bright star requires a planet-to-star contrast of $10^{-5} - 10^{-6}$ for young planets in the infrared. Developments in observing modes and post-processing have made us more sensitive to detecting these faint sources. One such image processing development is principal component analysis (PCA: Amara & Quanz 2012; Soummer et al. 2012). This algorithm involves modeling and removing the stellar PSF, allowing a planet signal to shine through. This is achieved by removing linear combinations of principal components, generated from the data itself. We developed and applied our own python PCA pipeline to Fomalhaut narrow band 4.05 μm images from NACO/VLT obtained with the APP coronagraph. We performed a series of tests and determined that optimizing the number of principal components maximizes the signal-to-noise from a planet very close to its parent star. We demonstrate that our PCA pipeline is up to one magnitude more sensitive than the previous analysis method. This work appeared in Meshkat et al. (2014).

Chapter 3
The young nature of directly imaged planets makes them ideal candidates to study the late stages of planet formation. However, relatively few planets have been directly imaged. The reason for the few detections is a combination of factors, including instrument modes, target selection, and poor understanding of the frequency of giant planets.

The “Holey Debris Disk” project was created to determine if debris disks with gaps are signposts for planet formation. These gaps are predicted to be dynamically caused by planets (Chiang et al. 2009) accreting debris material as they form. We obtained data with NACO/VLT, LMIRCAM, CLIO, and NICI. In this chapter we present the analysis of six targets observed with NACO/VLT using the APP coronagraph and processed with our optimized PCA pipeline. We targeted bright debris disks with well covered infrared data, allowing us to model their SEDs. By comparing the inferred radius of the gaps with the sensitivity curves, we determined the upper limit on companions that could be carving out these disks. Though only 15 targets were observed with all the facilities combined, two planets were discovered: HD 95086 b (Rameau et al. 2013b) and HD 106906 b (Bailey et al. 2014). This work appeared in Meshkat et al. (2015)

Chapter 4
(Rameau et al. 2013b) reported the discovery of a 5 Jupiter mass planet around

the star HD 95086. Though confirmed to not be a background source, this point source was only detected in L'-band, leaving us unable to rule out foreground L or T dwarfs. In this chapter we analyze our complimentary H-band data from the NICI instrument on Gemini, which resulted in a significant non-detection. This non-detection in the deep dataset allowed us to place a strict color lower limit of $H - L' > 3.1 \pm 0.5$ mag, ruling out foreground L/T dwarfs and demonstrating just how red, dusty, and cloudy these young planets may be. This work appeared in Meshkat et al. (2013)

Chapter 5
We discovered a companion orbiting the F7V star HD 984 at ~9 AU in L'-band, as part of our A and F star survey. The companion was recovered in L'-band non-coronagraphic imaging data taken a few days later. The mass of direct imaged companions is usually inferred from the luminosity and theoretical evolutionary tracks (Baraffe et al. 2003; Allard et al. 2013; Chabrier et al. 2000), which are extremely sensitive to the age of the system. HD 984 is an F-star in the middle of its main sequence, making it particularly challenging to determine its age. It has been argued to be a kinematic member of the 30 Myr-old Columba group (Malo et al. 2013), however it is possible that HD 984 is a kinematic interloper. We independently estimated a main sequence isochronal age of $2.0^{+2.1}_{-1.8}$ Gyr which does not rely on this kinematic association. Based on the L'-band photometry alone, the two age extrema and the COND evolutionary models (Baraffe et al. 2003), we estimate the companion mass to be between 33 and 120 $\mathrm{M_{Jup}}$ (0.03-$0.11\mathrm{M_{\odot}}$). To break this degeneracy, we obtained SINFONI $H + K$ integral field spectroscopy data to re-detect and characterize the companion. We compared its spectrum with field dwarfs and concluded that the companion is best fit by an M6.0±0.5 dwarf. This discovery suggests that caution should be used when estimating the masses of companions. This work is submitted.

Chapter 6
We observed thirteen A- and F-stars searching for sub-stellar companions with the APP on NACO/VLT. In addition to new companion detections, we aim to set direct imaging constraints on the frequency of sub-stellar companions as a function of stellar mass. The occurrence of giant planets is often extrapolated from radial velocity results to direct imaging surveys, however these two detection methods may probe very different planet populations (Vigan et al. 2012). We detected three low-mass companions, including one new M-dwarf (see Chapter 5). We ran Monte Carlo simulations to place constraints on the planet occurrence models for solar and A-type stars. Based on our non-detection of substellar companions in this survey, we reject the A-type star planet frequency for $r_{cutoff} > 80$AU, with 95% confidence. We also compare APP coronagraphic data with non-coronagraphic data, in order to assess when the APP outperformed direct imaging. This work is submitted.

Chapter 7
We discuss the future of direct imaging, including new instruments, coronagraphs,

image processing techniques, and targets.

References

Acke, B., Min, M., Dominik, C., et al. 2012, A&A, 540, A125
Alexander, R., Pascucci, I., Andrews, S., Armitage, P., & Cieza, L. 2014, Protostars and Planets VI, 475
Alibert, Y., Mordasini, C., & Benz, W. 2011, A&A, 526, A63
Allard, F., Homeier, D., Freytag, B., et al. 2013, Memorie della Societa Astronomica Italiana Supplementi, 24, 128
Amara, A., & Quanz, S. P. 2012, MNRAS, 427, 948
Bailey, V., Meshkat, T., Reiter, M., et al. 2014, ApJL, 780, L4
Baraffe, I., Chabrier, G., Barman, T. S., Allard, F., & Hauschildt, P. H. 2003, A&A, 402, 701
Batalha, N. M., Rowe, J. F., Bryson, S. T., et al. 2013, ApJS, 204, 24
Bergin, E. A., & Tafalla, M. 2007, ARA&A, 45, 339
Biller, B. A., Close, L. M., Masciadri, E., et al. 2007, ApJS, 173, 143
Biller, B. A., Liu, M. C., Wahhaj, Z., et al. 2013, ApJ, 777, 160
Boley, A. C. 2009, ApJL, 695, L53
Boss, A. P. 1998, ApJ, 503, 923
Bowler, B. P., Liu, M. C., Shkolnik, E. L., & Tamura, M. 2015, ApJS, 216, 7
Brandt, T. D., McElwain, M. W., Turner, E. L., et al. 2014, ApJ, 794, 159
Brauer, F., Dullemond, C. P., & Henning, T. 2008, A&A, 480, 859
Burrows, A., Sudarsky, D., & Hubeny, I. 2004, ApJ, 609, 407
Burrows, A., Marley, M., Hubbard, W. B., et al. 1997, ApJ, 491, 856
Chabrier, G., Baraffe, I., Allard, F., & Hauschildt, P. 2000, ApJ, 542, 464
Chauvin, G., Lagrange, A.-M., Dumas, C., et al. 2004, A&A, 425, L29
Chauvin, G., Vigan, A., Bonnefoy, M., et al. 2015, A&A, 573, A127
Chiang, E., Kite, E., Kalas, P., Graham, J. R., & Clampin, M. 2009, ApJ, 693, 734
Desidera, S., Covino, E., Messina, S., et al. 2015, A&A, 573, A126
Fergus, R., Hogg, D. W., Oppenheimer, R., Brenner, D., & Pueyo, L. 2014, ApJ, 794, 161
Fortney, J. J., & Nettelmann, N. 2010, Space Science Reviews, 152, 423
Fressin, F., Torres, G., Charbonneau, D., et al. 2013, ApJ, 766, 81
Galicher, R., Rameau, J., Bonnefoy, M., et al. 2014, A&A, 565, L4
Guillot, T. 2005, Annual Review of Earth and Planetary Sciences, 33, 493
Hayashi, C. 1981, in IAU Symposium, Vol. 93, Fundamental Problems in the Theory of Stellar Evolution, ed. D. Sugimoto, D. Q. Lamb, & D. N. Schramm, 113–126
Heinze, A. N., Hinz, P. M., Kenworthy, M., et al. 2010a, ApJ, 714, 1570
Heinze, A. N., Hinz, P. M., Sivanandam, S., et al. 2010b, ApJ, 714, 1551
Hinkley, S., Oppenheimer, B. R., Soummer, R., et al. 2009, ApJ, 701, 804
Janson, M., Brandt, T. D., Moro-Martín, A., et al. 2013, ApJ, 773, 73
Johnson, J. A., Butler, R. P., Marcy, G. W., et al. 2007, ApJ, 670, 833

Kalas, P., Graham, J. R., & Clampin, M. 2005, Nature, 435, 1067

Kalas, P., Graham, J. R., Chiang, E., et al. 2008, Science, 322, 1345

Kenworthy, M., Quanz, S., Meyer, M., et al. 2010, The Messenger, 141, 2

Konopacky, Q. M., Barman, T. S., Macintosh, B. A., & Marois, C. 2013, Science, 339, 1398

Kraus, A. L., & Ireland, M. J. 2012, ApJ, 745, 5

Krijt, S., Ormel, C. W., Dominik, C., & Tielens, A. G. G. M. 2015, A&A, 574, A83

Kuzuhara, M., Tamura, M., Kudo, T., et al. 2013, ApJ, 774, 11

Lafrenière, D., Jayawardhana, R., & van Kerkwijk, M. H. 2008, ApJL, 689, L153

Lafrenière, D., Marois, C., Doyon, R., Nadeau, D., & Artigau, É. 2007a, ApJ, 660, 770

Lafrenière, D., Doyon, R., Marois, C., et al. 2007b, ApJ, 670, 1367

Lagrange, A.-M., Gratadour, D., Chauvin, G., et al. 2009, A&A, 493, L21

Lagrange, A.-M., Bonnefoy, M., Chauvin, G., et al. 2010, Science, 329, 57

Lin, D. N. C., Bodenheimer, P., & Richardson, D. C. 1996, Nature, 380, 606

Lissauer, J. J., Dawson, R. I., & Tremaine, S. 2014, Nature, 513, 336

Lyot, B. 1939, MNRAS, 99, 580

Malo, L., Doyon, R., Lafrenière, D., et al. 2013, ApJ, 762, 88

Marley, M. S., Fortney, J. J., Hubickyj, O., Bodenheimer, P., & Lissauer, J. J. 2007, ApJ, 655, 541

Marois, C., Lafrenière, D., Doyon, R., Macintosh, B., & Nadeau, D. 2006, ApJ, 641, 556

Marois, C., Macintosh, B., Barman, T., et al. 2008, Science, 322, 1348

Marois, C., Macintosh, B., & Véran, J.-P. 2010, in Society of Photo-Optical Instrumentation Engineers (SPIE) Conference Series, Vol. 7736, Society of Photo-Optical Instrumentation Engineers (SPIE) Conference Series

Matthews, B., Kennedy, G., Sibthorpe, B., et al. 2014, ApJ, 780, 97

Mayer, L., Quinn, T., Wadsley, J., & Stadel, J. 2002, Science, 298, 1756

Mayer, L., Wadsley, J., Quinn, T., & Stadel, J. 2005, MNRAS, 363, 641

Mayor, M., & Queloz, D. 1995, Nature, 378, 355

Meshkat, T., Bailey, V. P., Su, K. Y. L., et al. 2015, ApJ, 800, 5

Meshkat, T., Kenworthy, M. A., Quanz, S. P., & Amara, A. 2014, ApJ, 780, 17

Meshkat, T., Bailey, V., Rameau, J., et al. 2013, ApJL, 775, L40

Naud, M.-E., Artigau, É., Malo, L., et al. 2014, ApJ, 787, 5

Nielsen, E. L., Liu, M. C., Wahhaj, Z., et al. 2013, ApJ, 776, 4

Okuzumi, S., Tanaka, H., Kobayashi, H., & Wada, K. 2012, ApJ, 752, 106

Pollack, J. B., Hubickyj, O., Bodenheimer, P., et al. 1996, Icarus, 124, 62

Quanz, S. P., Amara, A., Meyer, M. R., et al. 2013, ApJL, 766, L1

Rameau, J., Chauvin, G., Lagrange, A.-M., et al. 2013a, A&A, 553, A60

—. 2013b, ApJL, 779, L26

—. 2013c, ApJL, 772, L15

Rasio, F. A., Tout, C. A., Lubow, S. H., & Livio, M. 1996, ApJ, 470, 1187

Rieke, G. H., Su, K. Y. L., Stansberry, J. A., et al. 2005, ApJ, 620, 1010

Rouan, D., Riaud, P., Boccaletti, A., Clénet, Y., & Labeyrie, A. 2000, PASP, 112, 1479

Safronov, V. S., & Zvjagina, E. V. 1969, Icarus, 10, 109
Skemer, A. J., Marley, M. S., Hinz, P. M., et al. 2014, ApJ, 792, 17
Soummer, R., Pueyo, L., & Larkin, J. 2012, ApJL, 755, L28
Spiegel, D. S., & Burrows, A. 2012, ApJ, 745, 174
Vigan, A., Patience, J., Marois, C., et al. 2012, A&A, 544, A9
Wahhaj, Z., Liu, M. C., Nielsen, E. L., et al. 2013, ApJ, 773, 179
Weidenschilling, S. J. 1977, MNRAS, 180, 57
Wyatt, M. C. 2008, ARA&A, 46, 339